The cutting behavior of cortical bone in different bone osten cutting angles and depths of cut

Yuanqiang Luo
Changsha University of Science and Technology - Yuntang Campus: Changsha University of Science and Technology

Yinghui Ren (rebecca_ryh@hnu.edu.cn)
Hunan University https://orcid.org/0000-0002-4841-2544

Yang Shu
Hunan University

Cong Mao
Changsha University of Science and Technology

Zhixiong Zhou
Hunan University

Zhuming Bi
Purdue University Fort Wayne

Original Article

Keywords: Bone cutting surgery, Orthogonal cutting models, Anisotropic materials, Chip formation, Crack initialization and propagation, Fracture toughness

Posted Date: February 24th, 2021

DOI: https://doi.org/10.21203/rs.3.rs-232708/v1

The cutting behavior of cortical bone in different bone osteon cutting angles and depths of cut

Yuanqiang Luo[a,b], Yinghui Ren[a,*], Yang Shu[a], Cong Mao[b], Zhixiong Zhou[a], ZhuMing. Bi[c]

[a] Department of Mechanical and Vehicle Engineering, Hunan University, Changsha 410082, China
[b] Hunan Provincial Key Laboratory of Intelligent Manufacturing Technology for High-performance Mechanical Equipment, Changsha University of Science and Technology, Changsha 410114, China
[c] Department of Civil and Mechanical Engineering, Purdue University Fort Wayne, Fort Wayne, IN 46805, U.S.A.
*Corresponding authors: Yinghui Ren, E-mail: rebecca_ryh@hnu.edu.cn. Tel.: +86 13548596452

Abstract:

Cortical bones are semi-brittle and anisotropic, this brings the challenge to suppress vibration and avoid undesired fracture in precise cutting processes in surgeries. In this paper, we proposed a novel analytical model to represent cutting processes of cortical bones, and we used to evaluate cutting forces and fracture toughness, and investigate the formations of chips and cracks under varying bone osteon cutting angles and depths. To validate the proposed model, the experiments are conducted on orthogonal cuttings over cortical bones to investigate the impact of bone osteon cutting angle and depth on cutting force, crack initialization and growth, and fracture toughness of cortical bone microstructure. The experimental results highly agreed with the prediction by the proposed model in sense that (1) curly, serrated, grainy and powdery chips were formed when the cutting angle was set as 0°, 60°, 90°, and 120°, respectively. (2) Bone materials were removed dominantly by shearing at a small depth of cut from 10 to 50 μm, and by a mixture of pealing, shearing, and bending at a large depth of cut over 100 μm at different cutting orientations. Moreover, it was found that a cutting path along the direction of crack initialization and propagation benefited to suppress the fluctuation of cutting force thus reduce the vibration. The presented model has theoretical and practical significance in optimizing cutting tools and operational parameters in surgeries.

Keywords: Bone cutting surgery; Orthogonal cutting models; Anisotropic materials; Chip formation; Crack initialization and propagation; Fracture toughness

1. Introduction

Bone cutting processes are very common in knee arthroplasties, dental implants and spine surgeries; however, a bone cutting process exposes the risk of bone cracks. Such cracks cause an instable screw insertion [1] or instable cutting process in orthopedic robotic surgeries [2]. To predict a crack initiation and propagation, it is critical to investigate bone cutting behavior in a bone cutting process. Note that cortical bones are more complicated than conventional metallic composites; a cortical bone consists of osteons (around 100 μm), harversian canals, interstitial lamellae, and boundaries of osteons and interstitial lamellas with the weakest bonds [3].

Many researchers have studied three-dimensional (3D, cutting direction across, parallel and transverse to the bone osteon orientation) bone-cutting processes with the consideration of the depth of cut and the osteon orientations relative to the cutting direction. For example, Jacobs et al. [4] investigated how the depth of cut, tool rake angle, and bone orientation relative to cutting direction affected the chip formation to obtain in smooth and segmented chips. Malkin et al. [5] observed that the bone materials were removed as chips due to fracture occurring at the cutting edge. Sugita and Mitsuishi [6,7] analyzed the crack propagation and proposed a cutting technique to reduce force and temperature of a cutting process. Liao and Axinte [8] investigated the condition of a transition from shear to fracture of material removals in a 3D orthogonal cutting model. Feldmann et al. [9] characterized the effect of the rake angle and the depth of cut on the cutting force, the temperature and the fracture of brittle bones. Bai et al. [10] rationalized the crack propagation and chip morphology at both of microstructure and sub-microstructure scales. The aforementioned studies confined the scope of investigation for depth of cut, rake angle, and three orthogonal cutting directions; few works were reported on the bone cutting behavior of cortical bones in an arbitrary cutting direction. Note that in a real orthopedic surgery, not all of cutting processes are performed along an orthogonal direction; for examples, a K-wire drilling insertion was performed obliquely to orthogonal directions [11], the self-centering drill in [12] made the cut on an inclined plane that was neither parallel or perpendicular to the orientation direction of bone. In regards to the impact of cutting direction on chip formation, Cseke and Heinemann [13] argued that the cutting direction affected the drilling force; it was worth to be investigated further. Liao et al. [14] developed a cutting model to predict cutting force and temperature subjected to a given cutting angle in bone milling. Due to anisotropy of bone materials, a slight change of the cutting angle relative to the bone orientation may alter the

mechanism of chip formation and crack propagation significantly; therefore, it is of importance to investigate cutting behaviors with a cutting angle other than three orthogonal directions.

To understand bone cutting behavior, the properties of cortical bone materials, in particular, fracture toughness, must be characterized. Fracture toughness describes the ability of the material in resisting crack initiation and propagation. Limited works were reported on the investigation of fracture toughness of cortical bones in orthogonal cutting: Feldmann et al. [9] presented a bone fracture toughness model when the bone material was cut in a perpendicularly. Bai et al. [15] compared the bone fractures in conventional and impact cutting and found that the impact cutting was able to reduce the fracture toughness of bones; their conclusions were based on the assumption that the cutting direction was in one of three orthogonal directions. How to affect fracture toughness in an arbitrary direction was not covered.

This work aimed to develop a cutting model subjected to an arbitrary cutting direction other than three orthogonal directions and a large depth of cut. A new fracture toughness model was proposed to analyze material removal processes. To validate the cutting model, experiments were conducted to observe chip formation, measure the cutting force and calculate fracture toughness accordingly.

Nomenclature

a	Crack length	h	Depth of cut
a_o	Initial crack length	I_1	Area moment of inertia in mode #1
a_p	Crack length of cutter to first bone osteon	I_3	Area moment of inertia in mode #3
a_w	Width of cut	I_4	Area moment of inertia in mode #4
A_1	Cross-sectional area in mode #1	M	Moment of force
A_4	Cross-sectional area in mode #4	U_1	Elastic strain energy in mode #1
d	Diameter of single bone osteon	U_s	Shear energy in mode #2
E_1	Elastic modulus in mode #1	U_3	Elastic strain energy in mode #3
E_2	Elastic modulus in mode #2	U_4	Elastic strain energy in mode #4
E_3	Elastic modulus in mode #3	U_{Fn}	Elastic energy produced by F_n
E_4	Elastic modulus in mode #4	U_{Fc}	Elastic energy produced by F_c
E_f	Friction energy	W	Work by external force
F_c	Horizontal cutting force	y	A deflection in mode #1
F_n	Vertical cutting force	θ	Bone osteon cutting angle
G_1	Bone fracture toughness in mode #1	γ	Tool rake angle
G_2	Bone fracture toughness in mode #2	σ_s	Shear stress
G_3	Bone fracture toughness in mode #3	σ_c	Stress in cutting direction
G_4	Bone fracture toughness in mode #4	Π_2	Fracture energy

2. Chip formation and fracture toughness in different cutting directions

To investigate the impact of cutting direction relative to bone osteon orientation, the cutting direction is described by a bone osteon cutting angle θ in Fig. 1. In this section, θ is set as a discrete value of 0°, 60°, 90°, and 120°, respectively, and the cutting scenarios were referred as mode #1, #2, #3, and #4, correspondingly. In mode #1 (Fig. 1(a)), θ was set to 0°, and the cutting direction was parallel to the bone osteon orientation. In mode #2 (Fig. 1(b)), θ was set to 60°, and the cutting direction was with an angle of 60° to the bone osteon orientation. In mode #3 (Fig. 1(c)), θ was set to 90°, and the cutting direction was perpendicular to the bone osteon orientation. In mode #4 (Fig. 1(d)), θ was set to 120°, and the cutting direction was with an angle of 120° to the bone osteon orientation.

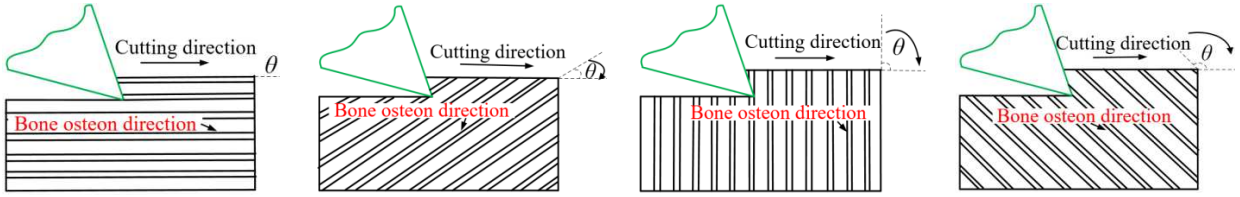

(a) (b) (c) (d)

Fig. 1. Bone orthogonal cutting modes: (a) mode #1, (b) mode #2, (c) mode #3, and (d) mode #4

Due to anisotropy and semi-brittle property of bones, the materials were removed dominantly by shears in a small depth of cut ranging from 10 to 60 μm, and the chips were continuous in any cutting direction (Liao et al. and Bai et al.[8,10]). When the depth of cut was increased over 100 μm, the bone removal behavior varied with the cutting direction relative of bone osteon orientation since cutting was made in the scale of osteons and haversian canals. A new model was needed to investigate chip formation, crack initiation and propagation, cutting force, and fracture toughness in different cutting directions.

2. 1 Mode #1 with a bone osteon cutting angle of 0°

In mode #1, the cutting direction was aligned with the bone osteon orientation, the cortical bone was removed along a cement line where the bone osteon and bone matrix were weakly joined. When a cutter inserted into cortical bone with a horizontal cutting force, crack a_0 was initiated, and the crack a was stably propagated during the cutting process. The thrust cutting force would accelerate the crack propagation along the cutting direction in Fig. 2(a). The

material removal was similar to peel a bone layer from the bone matrix, and the size of crack became (a_0+a).

The formed chip was simplified to a cantilever in Fig. 2 (b), and the chip was subjected to a bending moment by cutting forces F_n and F_c; this resulted in peeling a bone layer from the bone matrix. With a continuous cutting, the chip turned to a curly morphology in Fig. 2(c).

A fracture toughness model was developed based on the energy conservation principle in the cutting model; since the bone material was removed by the cutting force, and the work by the cutting force was converted into the elastic strain energy and potential energy, which was required to remove bone materials.

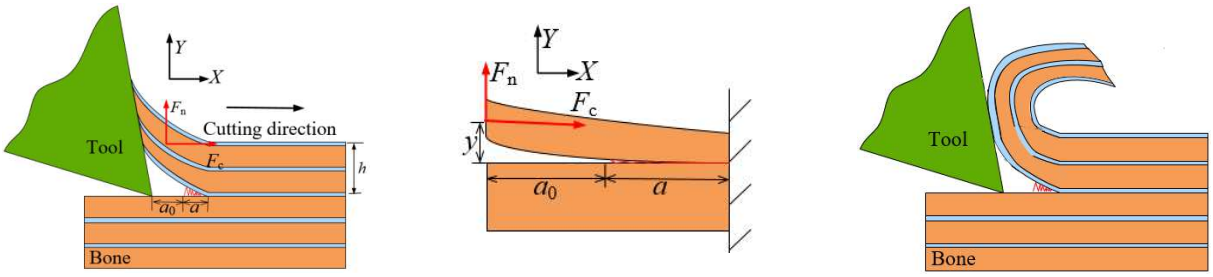

(a) (b) (c)

Fig. 2. Mode #1: (a) cutting model, (b) cutting force on bone osteon and (c) predicted chip morphology

Both of vertical and horizontal cutting force F_n and F_c contributed to elastic strain energy in the cutting process. The elastic strain energy by F_n was found as [17],

$$U_{F_n} = \frac{F_n^2 (a_0 + a)^3}{2E_1 I_1} \tag{1}$$

where E_1 was elastic modulus along to the bone osteon orientation; I_1 was the area moment of inertia calculated as,

$$I_1 = a_w h^3 / 12 \tag{2}$$

where h was the depth of cut, a_w was the width of cut.

The elastic strain energy by F_c was found as,

$$U_{Fc} = \frac{(F_c y)^2 (a_0 + a)}{2EI_1} \tag{3}$$

while y was the deflection at tip related to vertical cutting force F_n as,

$$y = \frac{F_n a^2 \left(2a + 3a_0\right)}{6EI_1} \tag{4}$$

Therefore, the total elastic strain energy U_1 in mode #1 was found as,

$$U_1 = U_{F_c} + U_{F_n} = \frac{F_c^2 F_n^2 a^4 \left(2a+3a_0\right)^2 \left(a_0 + a\right)}{72E_1^3 I_1^3} + \frac{F_n^2 \left(a_0+a\right)^3}{2E_1 I_1} \tag{5}$$

Assumed that the required potential energy for fracture was equal to the elastic strain energy [16], fracture toughness G_1 in mode #1 was determined by the elastic strain energy as,

$$\begin{aligned} G_1 &= \frac{1}{a_w}\frac{dU_1\left(a\right)}{da} \\ &= \frac{F_c^2 F_n^2 a^3 \left(28a^3 + 96a^2 a_0 + 105aa_0^2 + 36a_0^3\right)}{72a_w E_1^3 I_1^3} + \frac{3F_n^2 \left(a_0+a\right)^2}{2a_w E_1 I_1} \end{aligned} \tag{6}$$

The crack length was determined by [18],

$$a + a_0 = \sqrt{\frac{\pi^2 E_1 I_1}{4F_c}} \tag{7}$$

In eq. (6), since a_0 or a was very small, the first part could be ignored since the polynomial powers of a_0 and a were 6 and the resulted value of the first part would be insignificant in comparison with the result of the second part. Substituting eq. (7) into eq. (6) simplified the expression of the fracture toughness as,

$$G_1 = \frac{3\pi^2 F_n^2}{8a_w F_c} \tag{8}$$

2.2. Mode #2 with a bone osteon cutting angle of 60°

In mode #2, the bone osteon cutting angle θ was 60°, the material was removed alone the osteon orientation due to the weak strength at the cement line. The rake face of the tool pushed and deformed the material as serrated chips, and then the shear angle tended to close to the bone osteon cutting angle θ [19,20]. The bone material was cut away at the tool tip, which was similar

to the case when a ductile metal was removed in a cutting process. As shown in Fig. 3, the bone chip slipped along the shearing direction and deformed as serrated morphologies. The cracks were along the horizontal cutting force in the feeding direction. When the crack propagated from one osteon to the next, it propagated along the bone osteon orientation and penetrated with a small depth due to the horizontal pushing force.

For energy conservation, the total energy was from the work by the cutting force, and it was then converted into shear energy, friction energy and fracture energy.

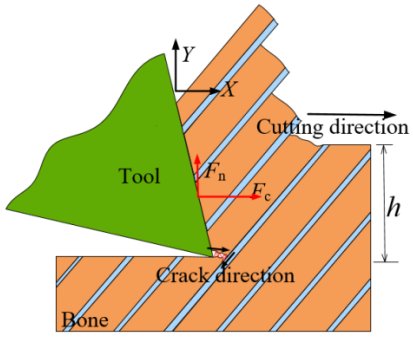

Fig. 3. Cutting model in mode #2

The condition for energy conservation was expressed by Patel et al. [21] as,

$$W = U_s + E_f + \Pi_1 \tag{9}$$

where U_s was the shear energy, E_f was the friction energy and Π_1 is the fracture energy in mode #2.

Eq. (9) could be deduced further as,

$$\frac{\sigma_s}{2}\frac{h}{\sin\theta} = \left(\frac{F_c}{a_w} - G_2\right)\cos\theta - \frac{F_n}{a_w}\sin\theta \tag{10}$$

where σ_s was the shear stress, h was the depth of cut, a_w was the width of cut, G_2 was the fracture strength, and F_c and F_n were cutting and thrust forces, respectively.

The fracture toughness was expressed as,

$$G_2 = \frac{F_c}{a_w} - \frac{\sigma_s}{2}\frac{h}{\sin\theta\cos\theta} - \frac{F_n}{a_w}\tan\theta \tag{11}$$

2. 3 Mode #3 with a bone osteon cutting angle of 90°

The cutting direction was perpendicular to the bone osteon orientation in mode #3. The bone osteon would be bended and cracked by F_c, and the initialized crack was propagated by the effect of F_n and F_c. In Fig. 4(a), bone osteons were cut down by F_c and the crack a occurred to the cutting direction. Due to a weak strength at the cement line of bone, cracks would be initialized in this boundary by the thrust force F_n. Fig. 4(b) showed the cutting and thrust force that are applied on a bone osteon, the cutting force mainly cut down the bone osteon and move it one by one. The removed bone osteons turned into grainy chips that were scattered over the bone surface showed in Fig. 4(c). Therefore, the chips in mode # 2 had grainy and scattered morphology.

The energy conservation principle was used to analyze a fracture toughness approximately.

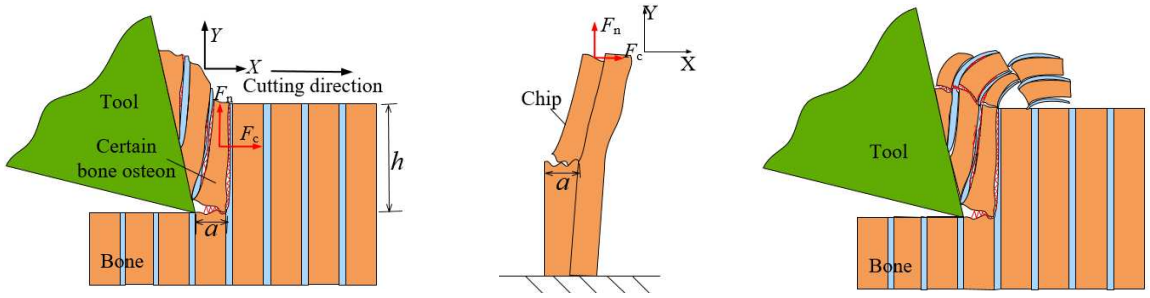

Fig. 4. Mode #3: (a) cutting model, (b) forces applied on a bone osteon and (c) predicted chip morphology

The elastic strain energy U_{Fn} by the thrust force was determined as [17,22],

$$U_{Fn} = \frac{1}{2}\frac{F_n^{\,2}h}{E_3 A} = \frac{F_n^2 h}{2E_3 A} \tag{12}$$

where E_3 was elastic modulus of bone osteon perpendicular to the cutting direction.

While the elastic strain energy U_{Fc} by cutting force was expressed as,

$$U_{F_c} = \frac{F_c^2 h^3}{2E_3 I_3} \tag{13}$$

The elastic strain energy U_3 was expressed as,

$$U_3 = U_{F_c} + U_{F_n} = \frac{F_n^2 h}{2E_3 A} + \frac{F_c^2 h^3}{2E_3 I_3} \tag{14}$$

Similar to the case in mode #1, the fracture toughness was calculated as,

$$G_3=\frac{U_3}{a_w a}=\frac{F_n^2 h}{2a_w a E_3 A}+\frac{F_c^2 h^3}{2a_w a E_3 I_3} \tag{15}$$

where a was the crack length that was around the diameter d = 118 μm of bone osteon in Fig. 4(b) [23], A = $d \times a_w$, I_3= $a_w \times d^3/12$ was the area moment of inertia.

2.4 Mode #4 with a bone osteon cutting angle of 120°

In mode #4, the cutting direction was opposite to the bone osteon orientation at a 120° angle. As shown in Fig. 5(a), the rake face of the tool touched the bone osteon earlier than the tool tip, and the bone osteon was bended and fractured due to the horizontal cutting force. The cutting process could be viewed to push and break bone osteons to produce the main crack a by the cutting force. Therefore, a bone osteon was modeled as a cantilever that was subjected to the cutting force.

Due to the brittleness of the bone materials, the bone osteon was crushed when the rake face made its contact, and the crushed bone materials turned into powdery morphologies in cutting process in Fig. 5(c).

The energy conservation principle was used to estimate the fracture toughness. The crack length a in Fig. 5(b) was calculated as,

$$a_p = h\left[\cot(\pi-\theta)-\tan\gamma\right] \tag{16}$$

$$a = a_p + d \tag{17}$$

where γ was an angle of tool rake angle.

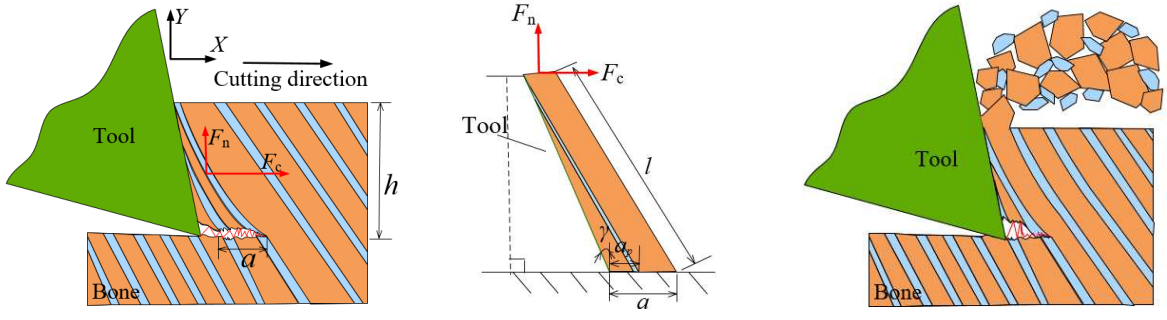

(a) (b) (c)

Fig. 5. Mode #4: (a) cutting model, (b) cutting forces on bone osteon and (c) predicted chip morphology

The elastic strain energy U_{Fn} by the thrust force was found as [17],

$$U_{F_n} = \frac{F_n^{\,2} h}{2E_4 A_4} \tag{18}$$

where E_4 was the elastic modulus, A_4 was the area, and $A_4 = a_w \times (d + d + a_p)/2$.

The elastic strain energy U_{Fn} by the cutting force was [17],

$$U_{F_c} = \frac{F_c^2 h^3}{2E_4 I_4} \tag{21}$$

where I_4 was the area moment of inertia of the bone osteon calculated as,

$$I_4 = \frac{a_w}{12}\left(\frac{d + d + a_p}{2}\right)^3 \tag{22}$$

Therefore, the total elastic strain energy U_4 was,

$$U_4 = \frac{F_n^2 h}{2E_4 A} + \frac{F_c^2 h^3}{2E_4 I_4} \tag{23}$$

Finally, the fracture toughness G_4 was calculated as,

$$G_4 = \frac{U_4}{a_w a} = \frac{F_n^2 h}{2a_w a E_4 A} + \frac{F_c^2 h^3}{2a_w a E_4 I_4} \tag{24}$$

3. Experiments

To validate the proposed cutting model in predicting chip morphology and fracture toughness in any cutting direction, orthogonal cutting experiments were conducted with varying cutting angles and depths of cut. The cutting tests were repeated four trials for a combination of a specified depth of cut and bone osteon cutting angle in Table 1.

Table 1 The parameters of orthogonal cutting experiments

Parameters	Value
Depth of cut h (μm)	10, 50, 90, 130
Bone osteon cutting angle θ (°)	0, 60, 90, 120

Due to the similar properties to human bones, bovine femur bones were commonly used in bone cutting experiments [24]. To prepare bone osteons for a cutting angle of 60° or 120°, fresh bovine femur bones were sawed to small pieces manually; pieces were then grounded to produce bone blocks with an inclined face of a 60° angle. As shown in Fig. 6(a), three machined faces were name as Face #1, #2 and #3, respectively. In each mode, the face with corresponding bone osteon orientation was set as cut face. To meet the condition of orthogonal cutting, the width of the cutter was wider than the width of cut. Thus, the bone block was sliced with a width of 2.5 mm in parallel to Face #1, #2 and #3, respectively. The width of the cutter had a width of 2 mm in Fig. 6(b). The prepared bones were stored in refrigerator.

To acquire stable cutting forces and chip morphologies in four modes with a different depth of cut, a micro-cutting setup was used to perform orthogonal cutting experiments in Fig. 6(c). Two active linear stages (Y axis and Z axis) (Model 200cri, Siskiyou Instrument) were mounted on the third active linear stage (X axis) (Model HLD 60, Moog Animatics). A precision micro-linear stage (Z' axis) (Model Micro-Controle, Klinger) was mounted on the Z axis linear stage to provide precise feeding. The cutter (Thinbit) had its rake and rear angles of 10° and 15°, respectively; it was clamped on the precision Z' axis to conduct these experiments. The cutting speed was set as 0.5 mm/s. A prepared bone was taken from the refrigerator and immerged into the saline for 2 hours at room temperature, and was then clamped on the worktable by a step block clamp.

In addition, the micro-cutting system was equipped with (1) a piezoelectric dynamometer (Model 9256C, Kistler) to measure cutting forces, (2) a data recorder (Model DL750 ScopeCorder, Yokogawa) to record force data with the sampling rate of 2000 Hz, and (3) a digital microscope (Model 503+, Gaosuo) to catch chip morphologies under different cutting conditions.

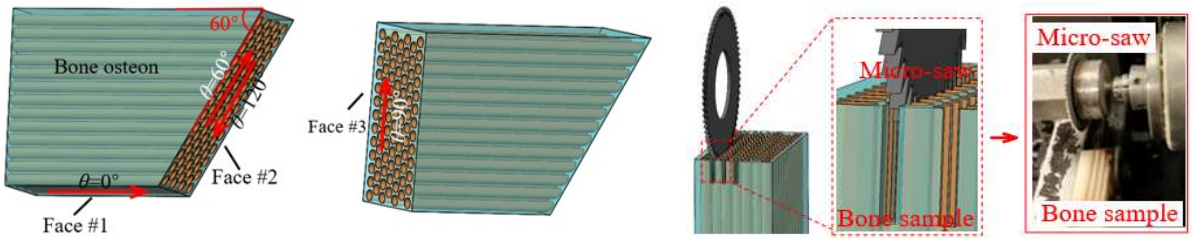

(a) (b)

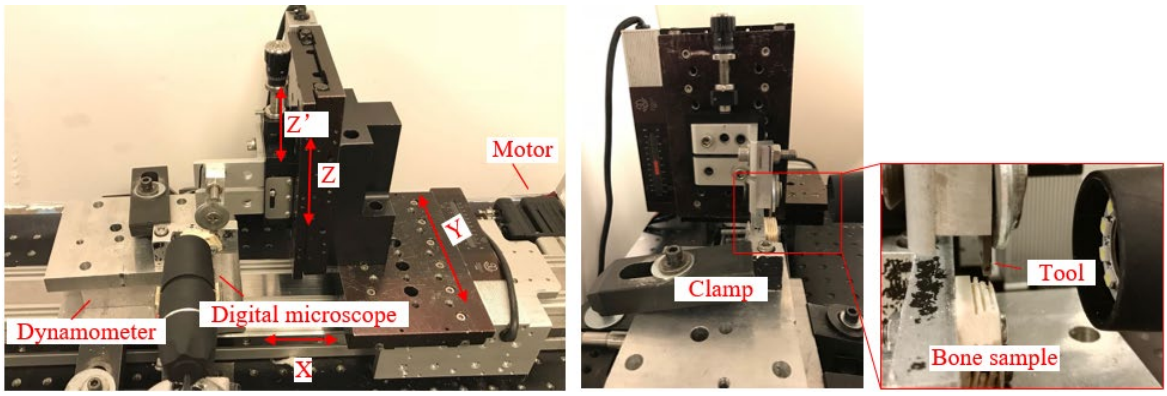

(c)

Fig. 6. Experimental setup for orthogonal cutting: (a) directions of bone osteons, (b) slicing over bones, and (c) data acquisition system.

4. Experimental results

Chip morphologies were captured by the digital microscope and the cutting forces under different cutting conditions were measured and recorded.

4.1. Chip morphologies

Fig. 7 showed the variety of chip morphologies in mode #1 (θ = 0°): Fig. 7(a) showed a continuous chip in a spiral shape under the depth of cut of 10 µm. Fig.7. (b) showed a continuous chip in a curvy shape under the depth of cut of 50 µm. Fig. 7 (c) showed a serrated chip under the depth of cut of 90 µm, and Fig. 7(d) showed a much curlier chip under the depth of cut of 130µm.

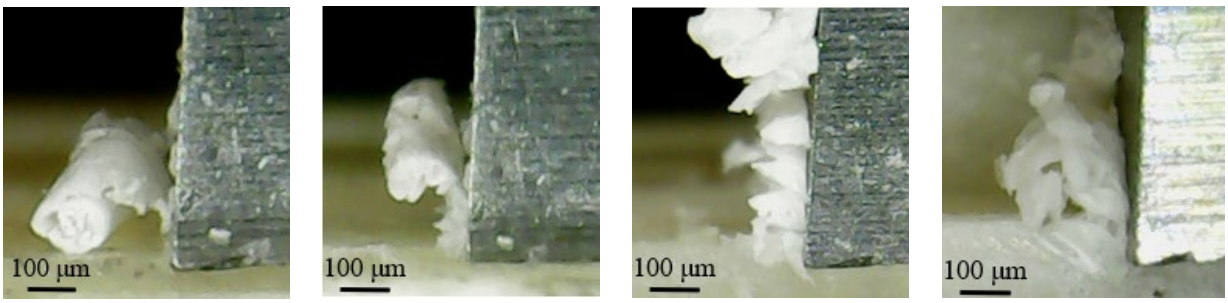

(a) (b) (c) (d)

Fig. 7. Chip morphologies (a) h=10 µm, (b) h= 50 µm, (c) h= 90 µm and (d) h= 130 µm in mode #1

When the cutting angle was set as 60° in mode #2, Fig. 8(a), (b), (c), and (d) showed the chip morphologies under the depth of cut of 10, 50, 90, and 130 µm, respectively.

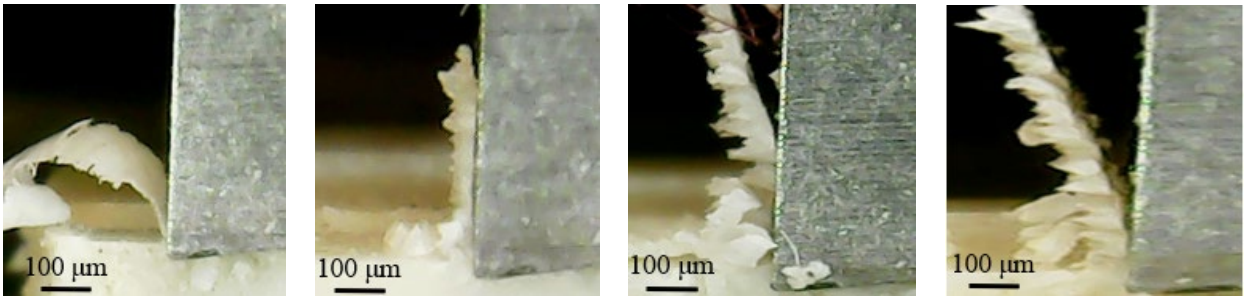

(a) (b) (c) (d)

Fig. 8. Chip morphologies (a) *h*=10 μm, (b) *h*= 50 μm, (c) *h*= 90 μm and (d) *h*= 130 μm in mode #2

When the cutting direction was perpendicular to the bone osteon orientation, Fig. 9(a) showed the continuous chip under the depth of cut of 10 μm. The chip became serrated when the depth of cut was set as 50 μm in Fig. 9(b). The chip became discontinued when the depth of cut was set as 90 μm in Fig. 9(c). At the depth of cut of 130 μm, the chip became large grainy as shown in Fig. 9(d).

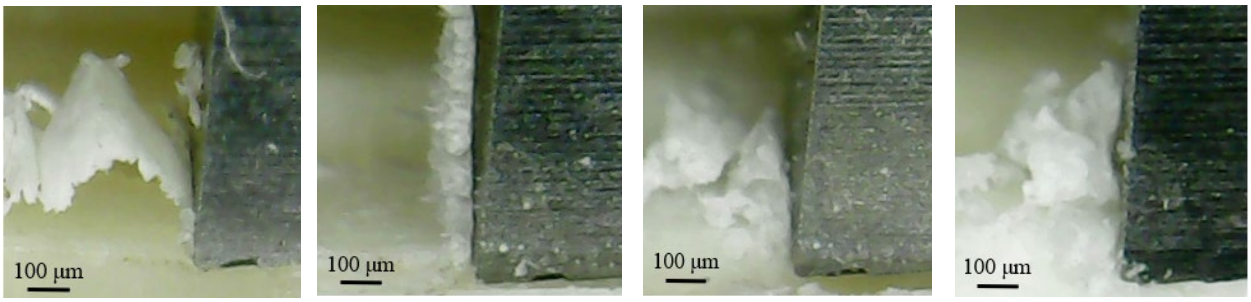

(a) (b) (c) (d)

Fig. 9. Chip morphologies (a) *h*=10 μm, (b) *h*= 50 μm, (c) *h*= 90 μm and (d) *h*= 130 μm in mode #3

When the bone osteon cutting angle was set as 120°, the cutting direction was opposite to the bone osteon orientation. With a depth of cut of 10μm, the chip in Fig. 10(a) was still continuously but tended to be broken easily. With a depth of cut of 50μm, the chip in Fig. 10(b) became continuous. With a depth of cut larger than 90μm, the chips in Figs. 10(c) and (d) were crushed powdery.

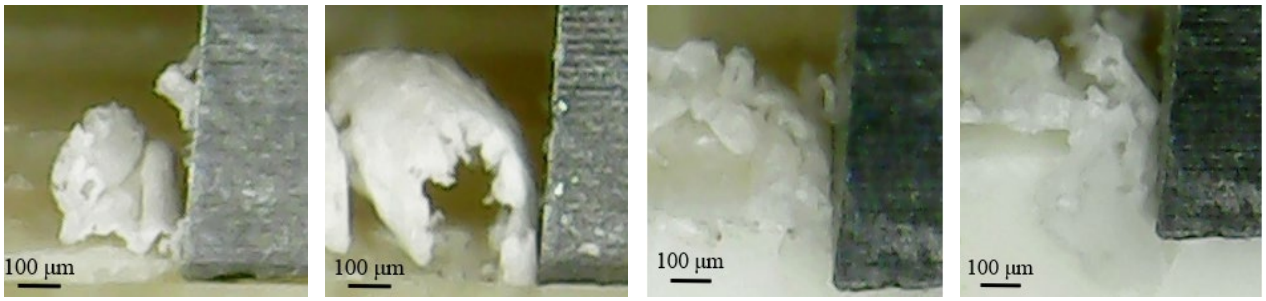

(a) (b) (c) (d)

Fig. 10. Chip morphologies (a) h=10 μm, (b) h= 50 μm, (c) h= 90 μm and (d) h= 130 μm in mode #4

4.2. Cutting force

Fig. 11 showed the cutting forces when the depth of cut was set as 10 μm in four cutting modes. Figs. 11(a) and (b) showed that the horizontal and vertical cutting forces in mode #1 and 2 were relatively stable; while the cutting forces in Fig. 11(c) and (d) for mode #3 and 4 showed obvious fluctuating.

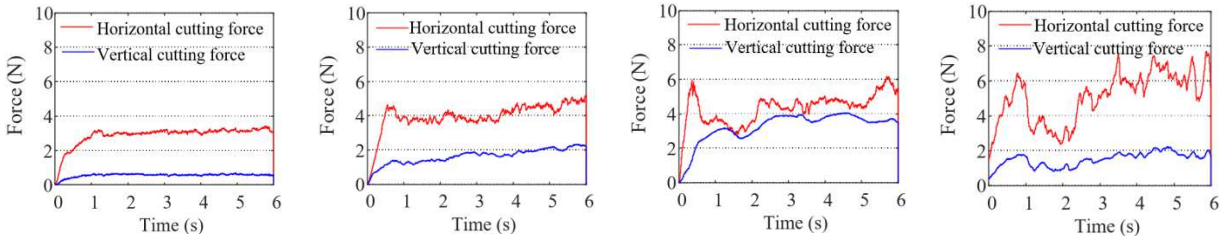

(a) (b) (c) (d)

Fig. 11. Cutting forces with the depth of cut of 10 μm: (a) mode #1, (b) mode #2, (c) mode #3, and (d) mode #4

Fig. 12 showed the cutting forces when the depth of cut was set as 130 μm in four cutting modes. A cutting force was characterized as its static and amplitude components. Although the static horizontal cutting force in any of these four modes remained constant, the amplitude of horizontal cutting force was increased when the cutting angle was increased from Fig. 12(a) to (d).

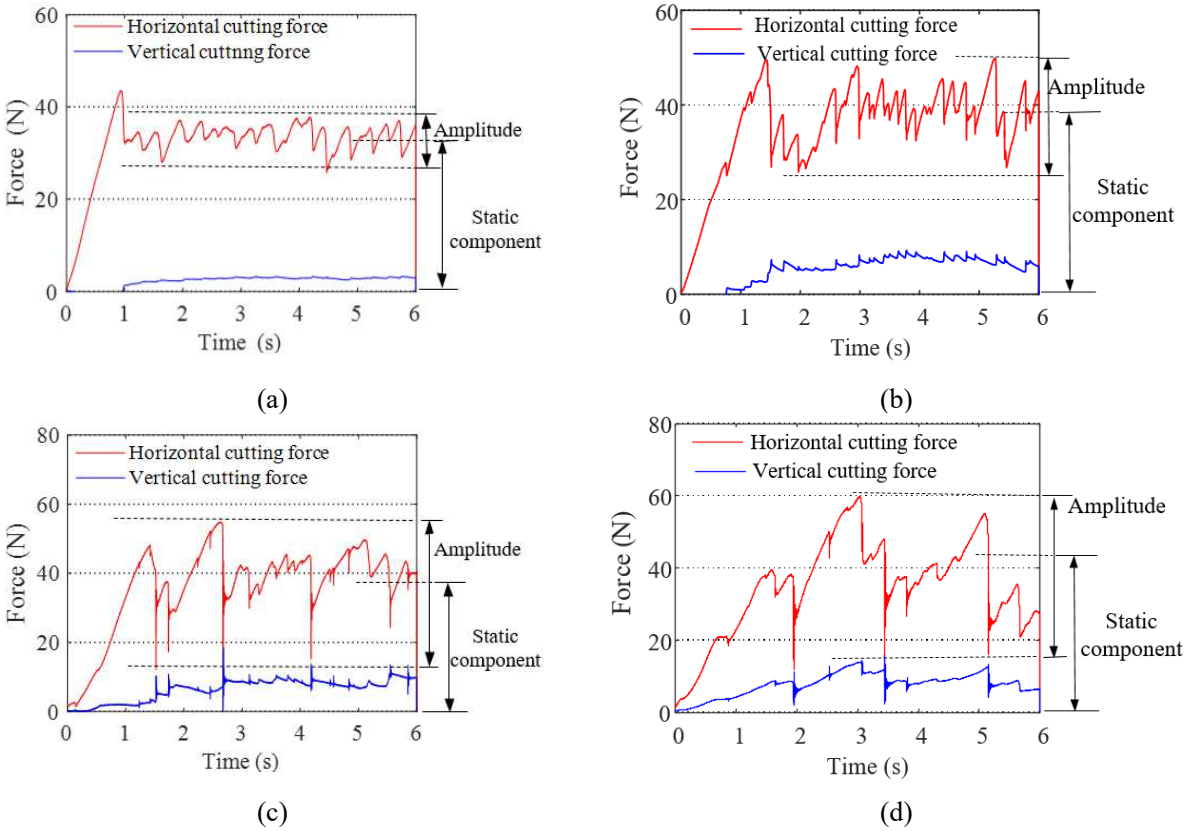

Fig. 12. Cutting forces with the depth of cut of 130 μm: (a) mode #1, (b) mode #2, (c) mode #3, and (d) mode #4

Fig. 13 compared the static horizontal and vertical cutting forces in different depths of cut. The solid lines were fitted by linear least squares. From the scatter dots in the depth of cut of 10 μm, the mean horizontal forces exhibited the same changing trend and increased with an increase of the cutting angle or the depth of cut shown in Fig. 13(a). The depth of cut and cutting angle also affect the static vertical cutting forces significantly shown in Fig. 13(b).

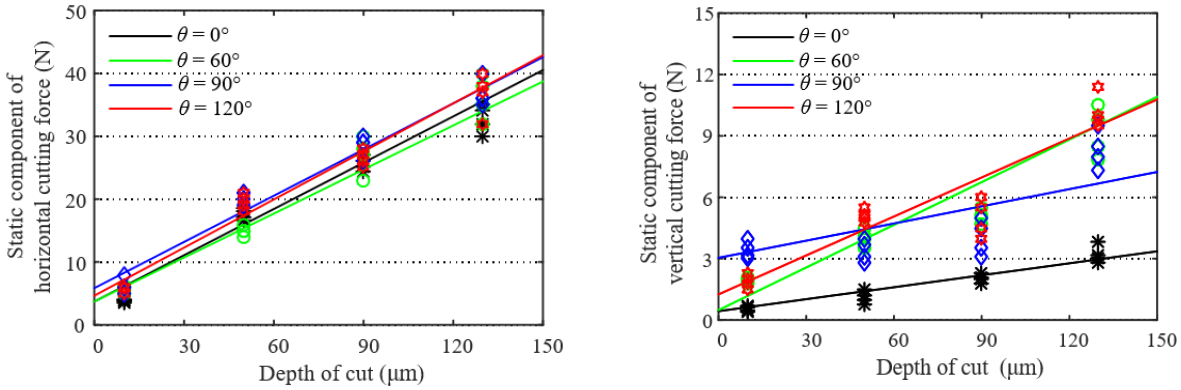

Fig. 13. Static component of cutting force versus the depth of cut

4.3 Fracture toughness

The bone fracture toughness could be calculated based on the static components of cutting force from bone orthogonal cutting experiments in four modes. While the elastic modulus in different bone osteon cutting angles is listed in Table 2. The shear stress σ_s in bone osteon cutting angle 60° is 67 $\times 10^6$ N/m^2 [25]. Thus, the values of fracture toughness in different bone osteon cutting angles are 652 ± 184 N/m, 3105 ± 1310 N/m, 1695 ± 302 N/m and 1532 ±149 N/m, respectively. They are largely various in four modes due to the bone anisotropic property.

Table 2 Elastic modulus in different bone osteon orientations [25]

Parameter	Value			
Bone osteon cutting angle θ (°)	0	60	90	120
Elastic modulus ($\times 10^9$ N/m^2)	10.4(± 1.64)	12.8 (± 1.57)	23.1 (±3.18)	12.8 (± 1.57)

5. Discussion

The experiments showed that continuous chips were formed in any cutting angle when the depth of cut was set as 10 μm; no crack was observed in Fig. 7(a), 8(a), 9(a) and 10(a). This conclusion agreed with the results reported in literatures [8,10]. However, the morphologies of chip curls at the same depth of cut showed the difference when the cutting angle was changed; it was caused by the difference of fracture strains due to the anisotropy of bone materials.

When the depth of cut was smaller than 20 μm, the horizontal cutting force was stable with less fluctuating shown in Figs. 11(a) and (b). However, the cutting angle affected the fracture in sense that the cutter needed to cut down the bone osteon in a transverse or even slightly opposite direction, this explained the light vibrations of horizontal cutting forces in Figs. 11(c) and (d).

When the depth of cut was increased to 50 μm, the serrated chip indicated that the material was removed by shearing. This result agreed well with the conclusion in [8,10] that the serrated chip happened when the depth of the cut was in the range of (20 μm to 60 μm). Based on the experiments and theoretical models, shearing became the predominate material removal mechanism when the depth of cut was set in this range. The bone osteon orientation mainly affected curling of chips and slightly affected the horizontal cutting force.

When the depth of cut was set over 100 μm, bone-cutting behaviors were highly diversified. Taking an example of mode #1, the depth of cut was at the scale of the diameters of osteons or haversian canals, cutting could be viewed as peeling a bone later from the bulk materials. That bone layer was cut, curled, and turned into a chip over the tool rake face in Fig. 14(b). This confirmed that the cutting model in Fig. 14(a) for mode #1 was appropraite since the material was peeled from the bone matrix. Fig. 14 showed that this operating condition would lead to high quality surface finish and no risk of tool break due to steable cutting force [26].

In mode #2, the cutting angle affected the cutting behaviors significantly. The material was removed by shearing, and the chip was serrated since the tilted bone osteon formed a shearing angle with the cutting direction. While the rake face pushed the chip forward, the materials were squeezed to make itself continuously stretched to continued and serrated chip in shown in Figs. 14 (c) and (d).

In mode #3, the bone osteon cutting angle was set to 90°. The material was cut along the cutting direction since the external force was mainly applied along the cutting direction (see Fig. 4 (c)). However, the crack was produced along the bone osteon orientation since the bonding strength of bone osteon and bone matrix was weak, and the chip was generated with a grainy morphology (see Fig. 14(e). The experiments showed that the chip formation in Fig. 14(f) matched the results of theoretical analysis reported in [10]. Different from the title bone osteon in mode #2 (Fig. 14(c)), a tilt angle was beneficial to material removal by shearing. In the cutting condition of mode #3, bone materials was cut and formed grainy chips.

In mode #4, the bone osteon cutting angle was set as 120°, and Fig. 14(g) showed that the bone material removal process experienced bending and crushing simultaneously. Since the rake face touched the bone osteon in advance and this produced a compressive pressure on the bone material. The tool tip then made the contact to bone osteon in proceeding the cutting process. The chip was crushed to power morphology as shown in Fig. 14(h).

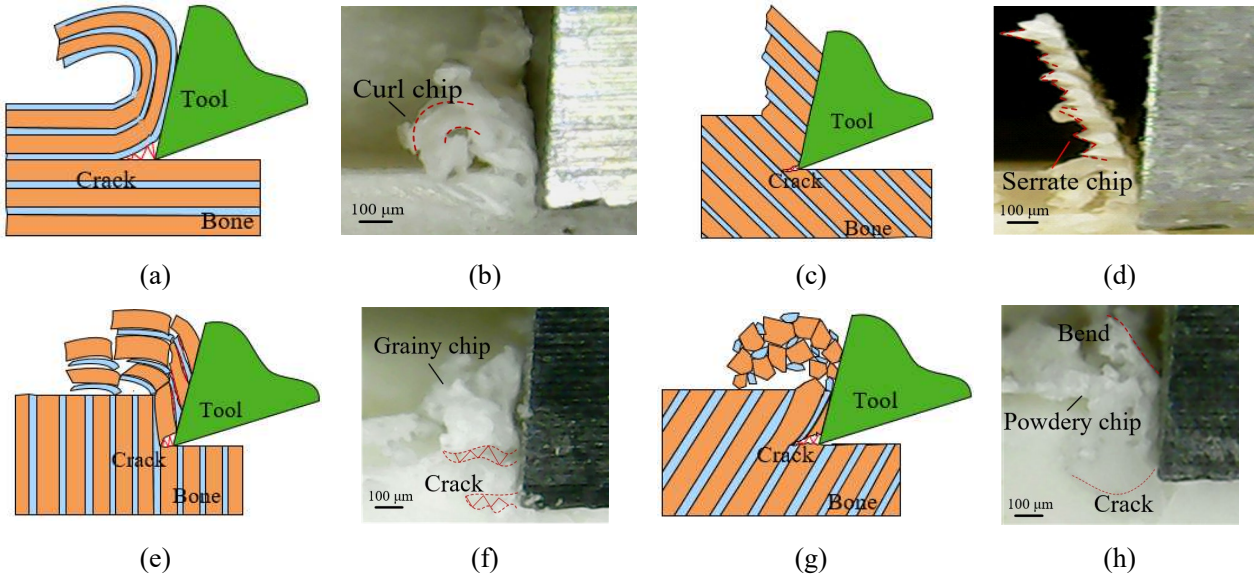

Fig. 14. Chip formations in depth of cut 130 µm: (a) cutting model for mode #1, (b) curl chip in mode #1, (c) cutting model for mode #2, (d) serrated chip in mode #2 (e) cutting model for mode #3, (f) grainy chip in mode #3, (g) cutting model for mode #4, and (h) powdery chip in mode #4

For the bone fracture toughness in mode #1, although the bone chip was peeling from the bone matrix, the material was fractured by an open mode [16]. While the fracture toughness was calculated to 652 ± 184 N/m. It was fairly close to the reported value 644 ± 102 N/m in [27]. For mode #2, no work was published on the fracture toughness of bone osteon at a cutting angle of 60°, the fracture model was shearing shown in Fig. 3. The fracture toughness was 1723 ± 487 N/m to 4710 ±1284 N/m at a cutting angle varying from 0° to 90° [27], and the fracture toughness for a cutting angle of 60° was 3105 ± 1310 N/m. In mode #3, the crack was produced perpendicularly to the bone osteon orientation, the fracture mechanism was an open mode, and the corresponding fracture toughness was 1495 ± 302 N/m. The deviation of fracture toughness was large since the cutting force was fluctuated sharply, the estimated fracture toughness was similar to the reported value 1532±149 N/m [27]. In mode #4, no work was reported for the corresponding fracture toughness. Since the cutter was slightly opposite to the bone osteon orientation, the required cutting energy in this mode was larger than that in mode #3, and the fracture toughness was slightly larger than that in mode #3.

The largest fracture toughness was mode #2 in a shearing model fracture, followed by mode #4, mode #3, and mode #1 in open mode fracture. Fig. 15 showed the correspondence of crack growth and propagation and dynamic cutting force. Since the fracture toughness was associated

with crack initiation and propagation, the fracture toughness was the lowest in mode #1, which meant that the crack in this mode was initialized and propagated easily in the left of Fig. 15(a). The crack was along the weak cement line in the cutting direction, and it produced a stable cutting force (see the enlarged view in the right of Fig. 15 (a)). For the shear mode fracture in mode #2, the crack was initialized and propagated hardly through the bone osteon and extended to the cement line with arrowed micro cracks in the left of Fig. 15(b). Since micro cracks were propagated faster than the cutter, when the cutter approached, a vibration force occurred (see the enlarged view in the right of Fig. 15(b)). In mode #3, the crack was initialized and propagated to the next bone osteon in advance, the direction of the crack propagation was perpendicular to the cutting direction as arrowed in the left side of Fig. 15(c). When the cutter arrived here, it produced a highly vibrated cutting force (see the enlarged view in the right of Fig. 15(c)), the amplitude of the horizontal force was larger than that in Fig. 15(b). Since the fracture toughness was smaller than that in mode #2, it easily produced a vertical crack to the cutting direction. In mode #4, a crack propagated to the next bone osteon and then extended along the weak cement line, which was stretched in machined surface deeply. Since the rake face of cutter touched the bone osteon in advance with a force, which accelerated the crack propagation along the cement line along the arrow shown in the left of Fig. 15(d). When the cutter arrived here, it produced more highly vibrated force (see the enlarged view in the right of Fig. 15(d)). A longer and deeper crack or a virbrated force produced powdery chip but affected the surface finish adversely [26].

In a summary, when the fracture toughness was small, and the crack was initilized and propagated along the cutting direction, it would produce a stable cutting force and result in high quality surface. In such an operating condition, the crack helped the material removal process. When the crack growth and propagation was not along the cutting direction, the frature toughness was increased to deccerlate crack propagation.

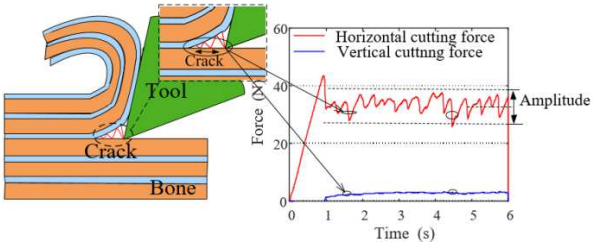

(a)

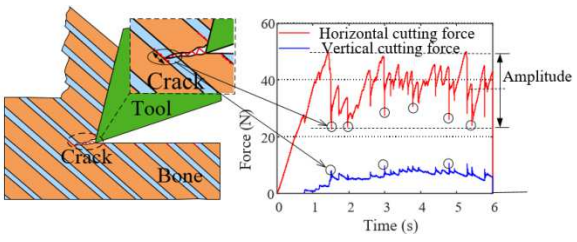

(b)

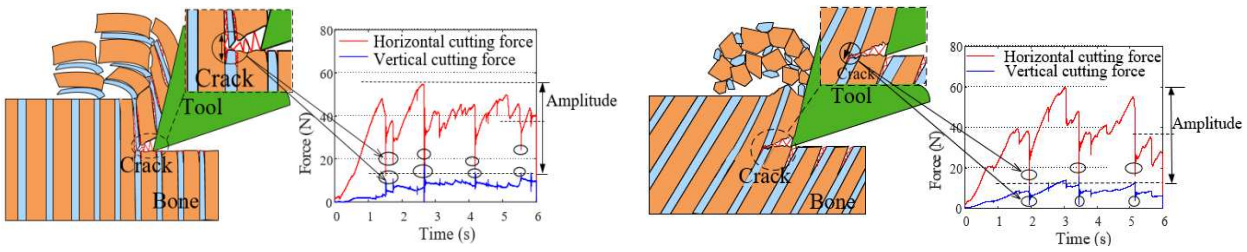

(c) (d)

Fig. 16. Crack propagations and cutting forces when the depth of cut was set as 130 μm: (a) mode #1, (b) mode #2, (c) mode #3 (d) mode #4

6. Conclusion

This work was motivated to optimize cutting parameters to suppress vibration and avoid undesired fracture in precise cutting processes in surgeries; in particular, the impact of the depth of cut and the cutting direction relative of bone osteon orientation on chip formation and fracture toughness were focused, the analytical models for four typical conditions were developed, and experiments were performed to show the effectives of the proposed models in predicting chip morphologies and cutting forces. It has been found that:

(1). The chip morphology was affected by the cutting direction relative to the bone osteon orientation and the depth of cut greatly. With a small depth of cut, the chip was continuous, and the curl radius of chip varied with the cutting angle. With a large depth of cut, the chip morphology became curly, serrate, grainy and powdery when the cutting angle was set as 0°, 60°, 90°, and 120°, respectively.

(2). The proposed cutting models and experiments showed that the bone cutting behavior was varied with the depths of cut and the cutting direction. In a small depth of cut up to 50 μm, the bone material was removed by shearing, and the impact of the cutting angle was insignificant. When the depth of cut reached over 130 μm, the cutting angle affected the cutting behavior greatly, and the materials were removed by peeling, shearing, cutting, and a mixture of bending and cutting at the cutting angle of 0°, 60°, 90°, and 120°, respectively.

(3). For a large depth of cut, the fracture toughness model was established and applied to estimate the fracture toughness under a varying angle. Using the acquired data from experiments, the fracture toughness was found as 652 ± 184 N/m, 3105 ± 1310 N/m, 1495 ± 302 N/m and 1532 ± 149 N/m at the cutting angle of 0°, 60°, 90°, and 120°, respectively.

(4). The cutting force was increased with the increase of bone osteon cutting angles. When the crack growth and propagation was along with the cutting direction, the fracture toughness was low and less cutting force was needed to remove a chip. When the crack growth and propagation was not in the direction of cutting, the fracture toughness was increased and it resists the crack propagation which is beneficial to bone machine.

The aforementioned findings have this theoretical and practical significance in helping engineers to design orthopedic tools and optimize operational parameters in bone-cutting surgeries.

Acknowledgements

Authors would like to thank the supports from University of Michigan, USA in experiments.

Author's Contributions

YL and YR designed experiments, acquired data and edited manuscript draft; YS assisted with experiments data analysis; CM, ZZ and ZB edited and supervised the manuscript. All authors read and approved the final manuscript.

Availability of Data and Materials

The datasets supporting the conclusions of this article are included within the article.

Funding

This study was sponsored by the China Scholarship Council and the National Natural Science Foundation of China (grant no. 52075161).

Competing Interests

The authors declare no competing financial interests.

References

[1] M Hollensteiner, S Sandriesser, E Bliven,et al. Biomechanics of Osteoporotic Fracture Fixation. *Current Osteoporosis Report,* 019,17: 363–374.

[2] L Bai, J Yang, X Chen, et al. Medical robotics in bone fracture reduction surgery: A review. *Sensors,* 2019, 19: 3593-3612.

[3] EA Zimmermann, ME Launey, RO Ritchie. The significance of crack-resistance curves to the mixed-mode fracture toughness of human cortical bone. *Biomaterials,* 2010, 20(31): 5297–5305.

[4] CH Jacobs, MH Pope, JT Berry, et al. A study of the bone machining process-orthogonal cutting. *Journal of Biomechanics*, 1974, 7: 131–136.

[5] S Malkin, KL Wiggins . Orthogonal Machining of Bone. *Journal of Biomechanics Engineering,* 2010, 100(3):122.

[6] N Sugita, M Mitsuishi. Specifications for machining the bovine cortical bone in relation to its microstructure. *Journal of Biomechanics*, 2009, 42(16): 2826–2829.

[7] N Sugita, T Osa, R Aoki, et al. A new cutting method for bone based on its crack propagation characteristics. *CIRP Annal - Manufacturing Technology*, 2009, 58(1): 113–118.

[8] Z Liao, DA Axinte. On chip formation mechanism in orthogonal cutting of bone. International *Journal of Machine Tools and Manufacture*, 2016, 102: 41–55.

[9] A Feldmann, P Ganser, L Nolte, et al. Orthogonal cutting of cortical bone: Temperature elevation and fracture toughness. International *Journal of Machine Tools and Manufacture*, 2017, 118–119: 1–11.

[10] W Bai, L Shu, R Sun,et al. Mechanism of material removal in orthogonal cutting of cortical bone. *Journal of Mechanical Behavior of Biomedical Materials*, 2020, 104.

[11] SA Brennan, C Kiernan, S Beecher, et al. Volar plate versus k-wire fixation of distal radius fractures. *Injury,* 2016, 47: 372–376.

[12] L Shu, S Li, M Terashima, et al. A novel self-centring drill bit design for low-trauma bone drilling. International *Journal of Machine Tools and Manufacture*, 2020, 154.

[13] A Cseke, R Heinemann. The effects of cutting parameters on cutting forces and heat generation when drilling animal bone and biomechanical test materials. *Medical Engineering and Physics*, 2018, 51: 24–30.

[14] Z Liao, D Axinte, D Gao. On modelling of cutting force and temperature in bone milling. *Journal of Materials Processing Technology*, 2019, 266: 627–638.

[15] W Bai, L Shu, R, Sun et al. Improvements of material removal in cortical bone via impact cutting method. *Journal of Mechanical Behavior of Biomedical Materials*, 2020, 108.

[16] TL Anderson. *Fracture mechanics: fundamentals and application*. Third. USA: CRC Press, 2005.

[17] Y Luo, L Gao, G Liu, et al. *Mechanics of materials*. China: Science press, 2004.(in Chinese)

[18] L Chen, K Zhang, H Cheng et al. A cutting force predicting model in orthogonal machining of unidirectional CFRP for entire range of fiber orientation. *The International Journal of Advanced Manufacturing Technology*, 2017, 89: 833–846.

[19] H Li, X Qin, G He et al. Investigation of chip formation and fracture toughness in orthogonal cutting of UD-CFRP. *The International Journal of Advanced Manufacturing Technology*, 2016, 82: 1079–1088.

[20] RO Ritchie, MJ Buehler, P Hansma. Plasticity and toughness in bone. *Physics Today*, 2009, 62: 41–47.

[21] Y Patel, BRK Blackman, JG Williams. Determining fracture toughness from cutting test on polymers. *Engineering Fracture Mechanics*, 2009, 76: 2711–2730.

[22] O Gavalda Diaz, DA Axinte. Towards understanding the cutting and fracture mechanism in ceramic matrix composites. International *Journal of Machine Tools and Manufacture,* 2017, 118–119:12–25.

[23] JP Morales, HI Roa, D Zavando, et al. Determination of the species from skeletal remains through histomorphometric evaluation and discriminant analysis. *International Journal of Morphology*, 2012, 30:1035–1041.

[24] P Geoeges, P Squire. Comparison of the mechanical properties of a new bone xenograft with human and bovine trabecular bone. *Orthopedie Traumatologie*, 1992, 2(4): 265–268.

[25] DT Reilly, AH Burstein, The elastic and ultimate properties of compact bone tissue, *Journal of Biomechanics*, 1975, 8: 393–493.

[26] P Huang, J Li, J Sun, et al. Vibration analysis in milling titanium alloy based on signal processing of cutting force. *The International Journal of Advanced Manufacturing Technology*, 2013, 64: 613–621.

[27] Z Feng, J Rho, S Han,et al. Orientation and loading condition dependence of fracture toughness in cortical bone. *Materials Science and Engineering:C*, 2000, 11(1): 41–46.

Figures

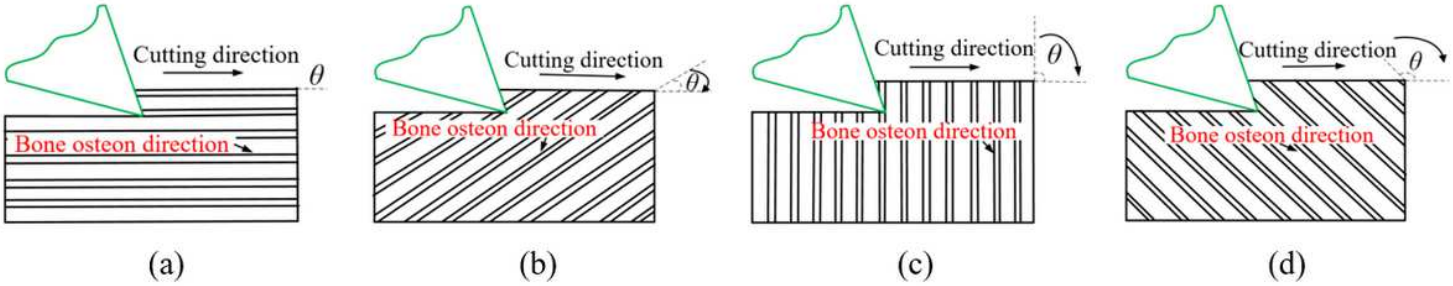

Figure 1

Bone orthogonal cutting modes: (a) mode #1, (b) mode #2, (c) mode #3, and (d) mode #4

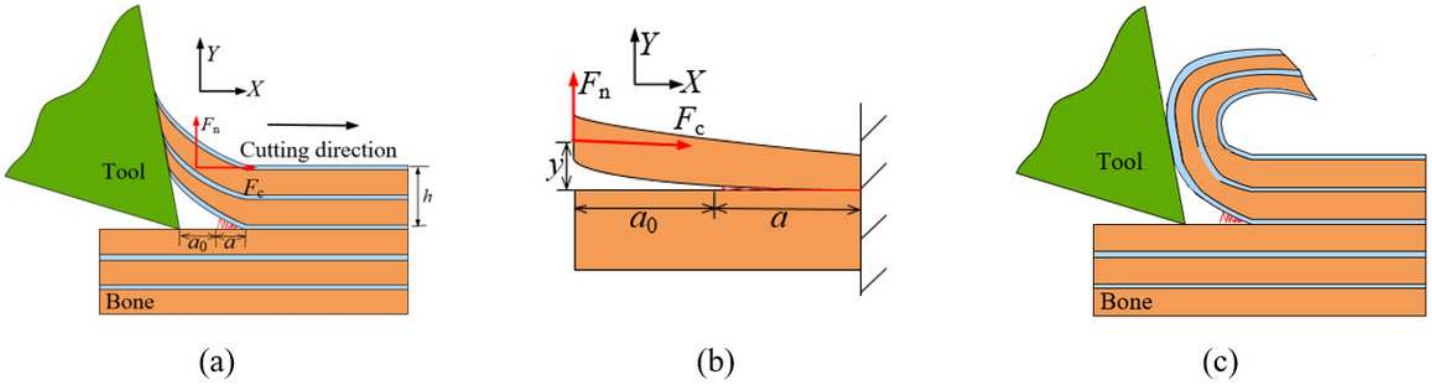

Figure 2

Mode #1: (a) cutting model, (b) cutting force on bone osteon and (c) predicted chip morphology

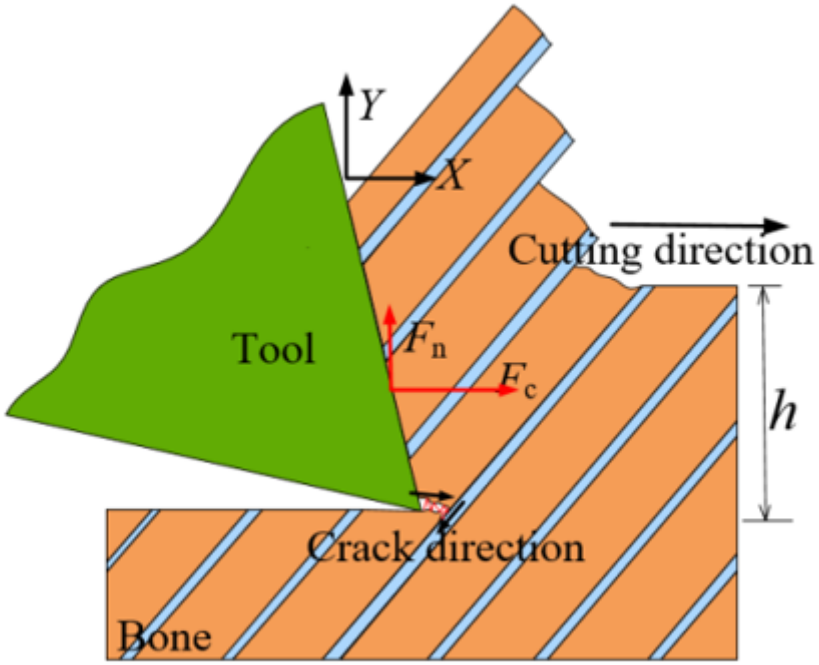

Figure 3

Cutting model in mode #2

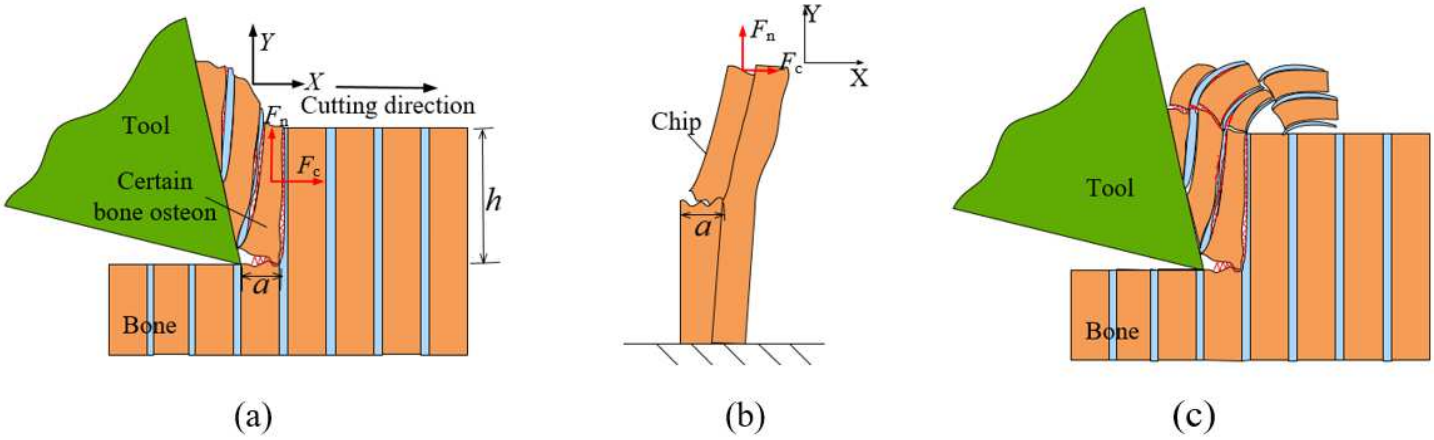

Figure 4

Mode #3: (a) cutting model, (b) forces applied on a bone osteon and (c) predicted chip morphology

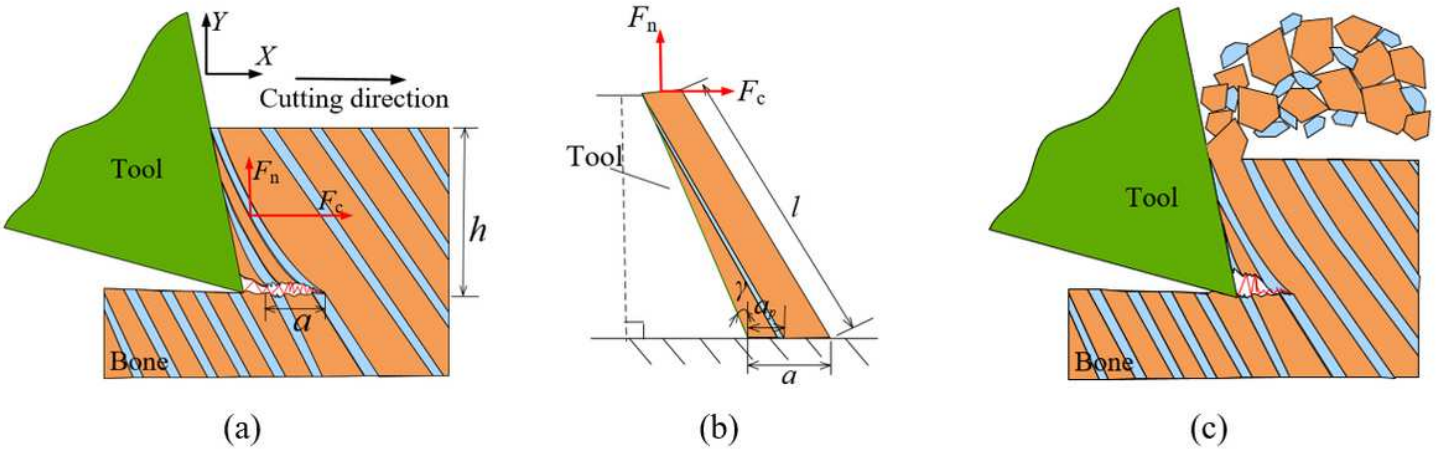

Figure 5

Mode #4: (a) cutting model, (b) cutting forces on bone osteon and (c) predicted chip morphology

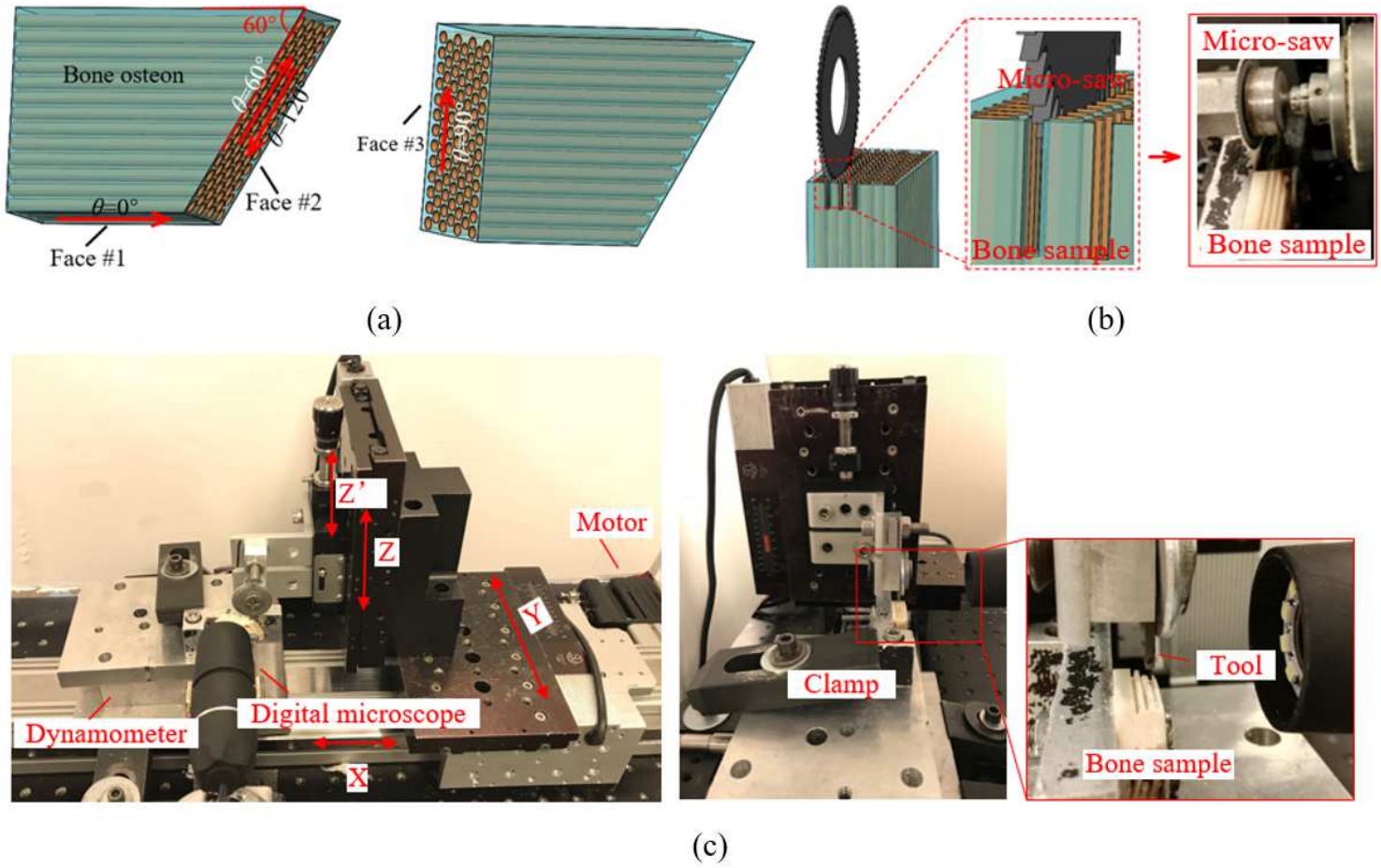

Figure 6

Experimental setup for orthogonal cutting: (a) directions of bone osteons, (b) slicing over bones, and (c) data acquisition system.

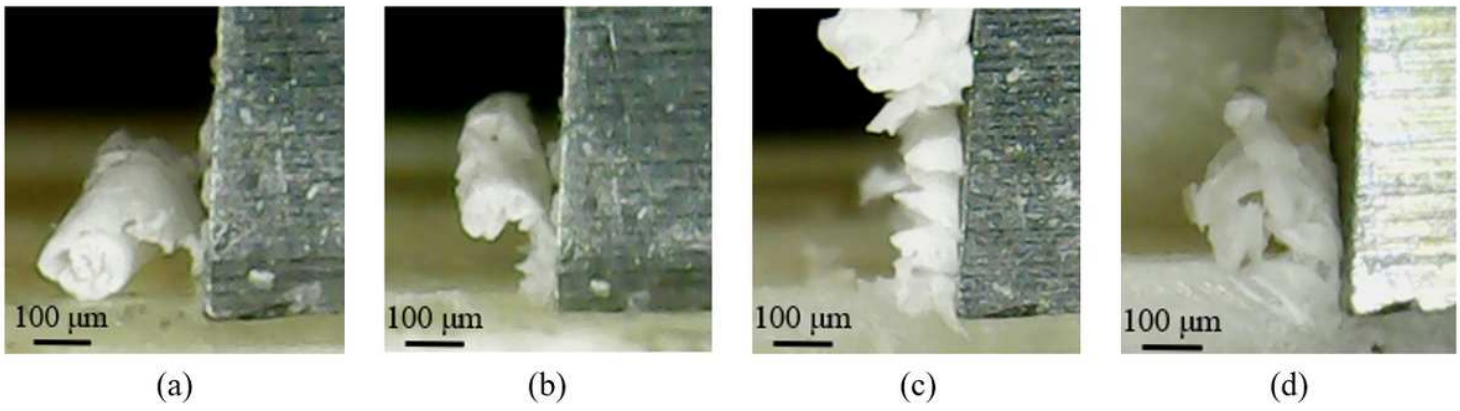

Figure 7

Chip morphologies (a) h=10 µm, (b) h= 50 µm, (c) h= 90 µm and (d) h= 130 µm in mode #1

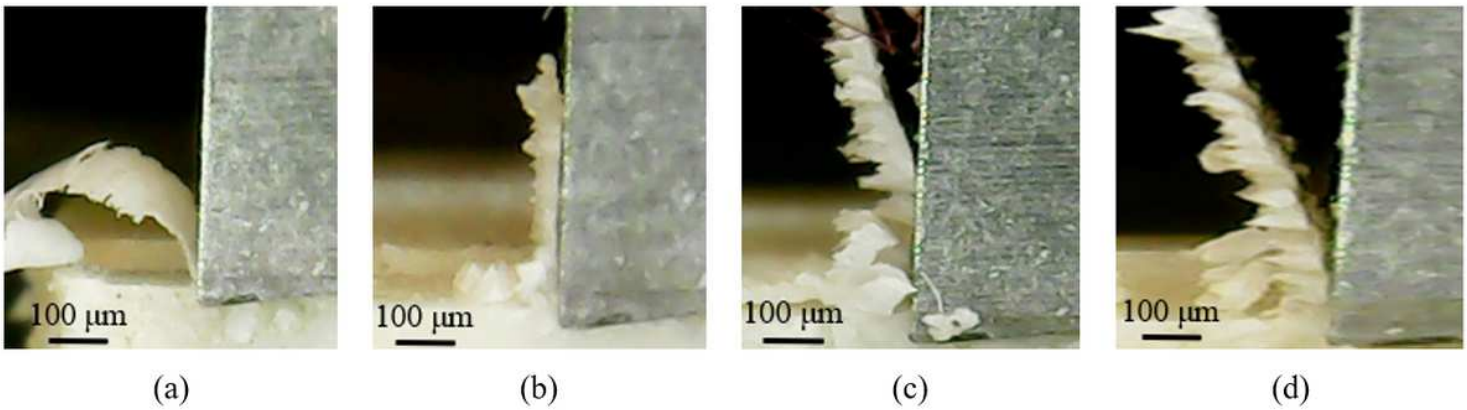

Figure 8

Chip morphologies (a) h=10 µm, (b) h= 50 µm, (c) h= 90 µm and (d) h= 130 µm in mode #2

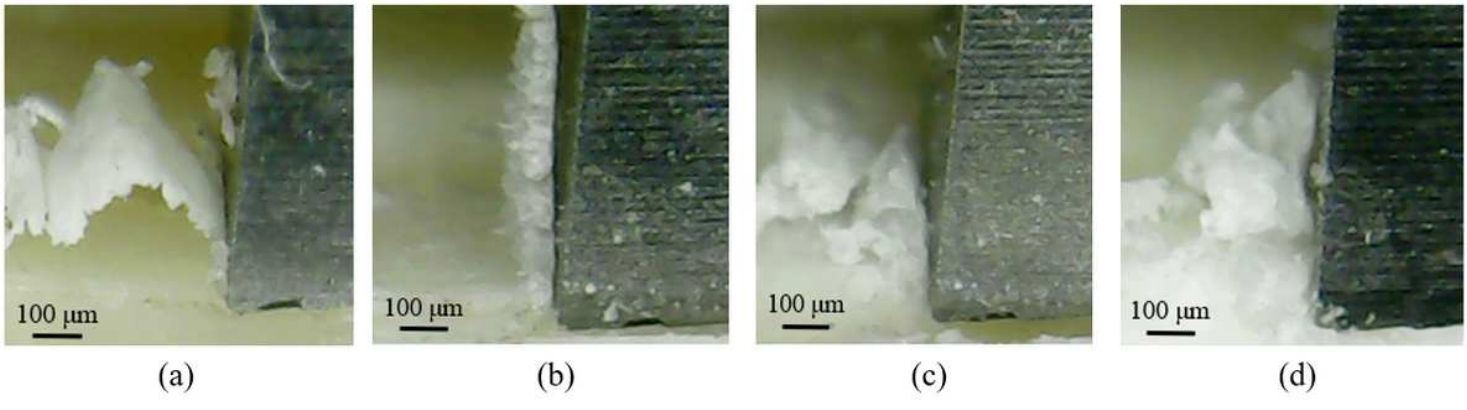

Figure 9

Chip morphologies (a) h=10 µm, (b) h= 50 µm, (c) h= 90 µm and (d) h= 130 µm in mode #3

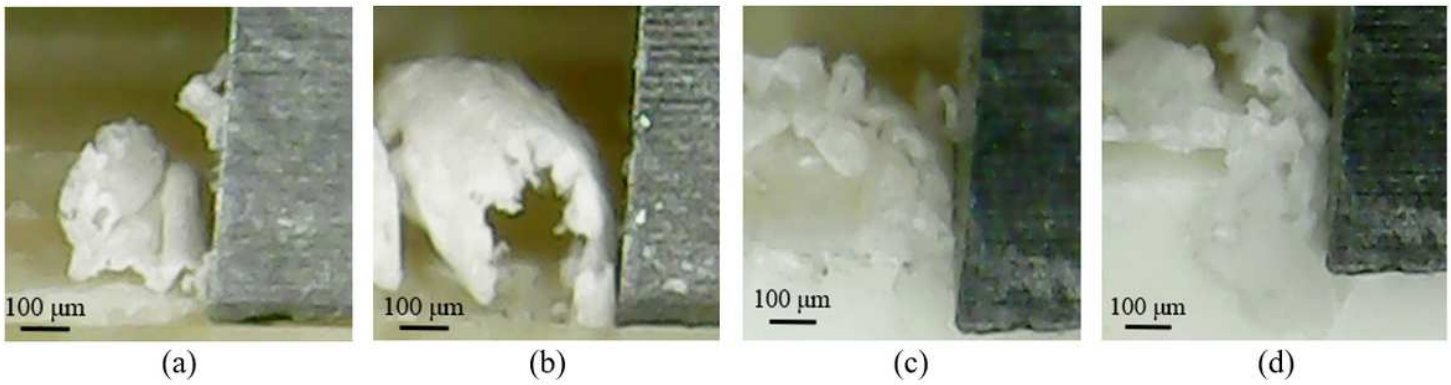

Figure 10

Chip morphologies (a) h=10 μm, (b) h= 50 μm, (c) h= 90 μm and (d) h= 130 μm in mode #4

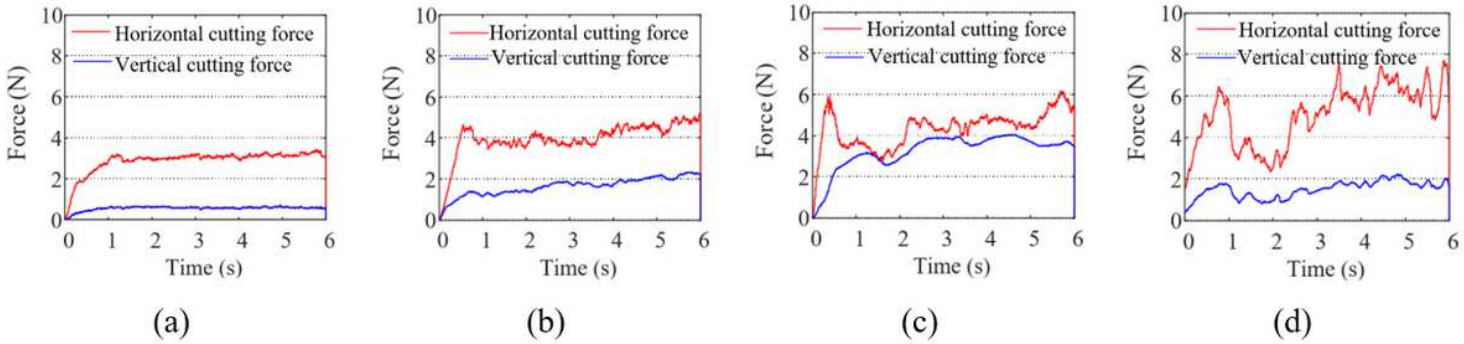

Figure 11

Cutting forces with the depth of cut of 10 μm: (a) mode #1, (b) mode #2, (c) mode #3, and (d) mode #4

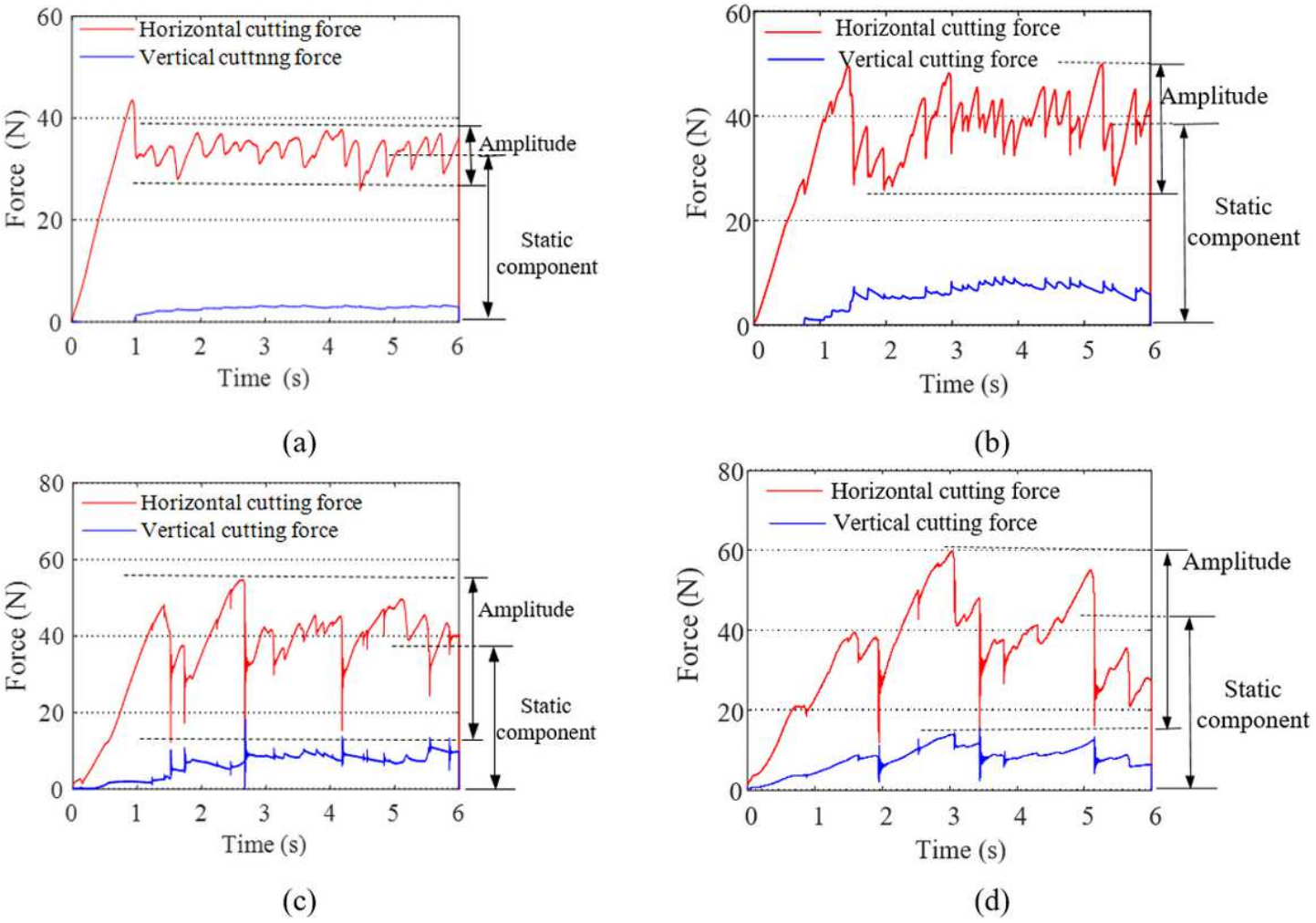

Figure 12

Cutting forces with the depth of cut of 130 μm: (a) mode #1, (b) mode #2, (c) mode #3, and (d) mode #4

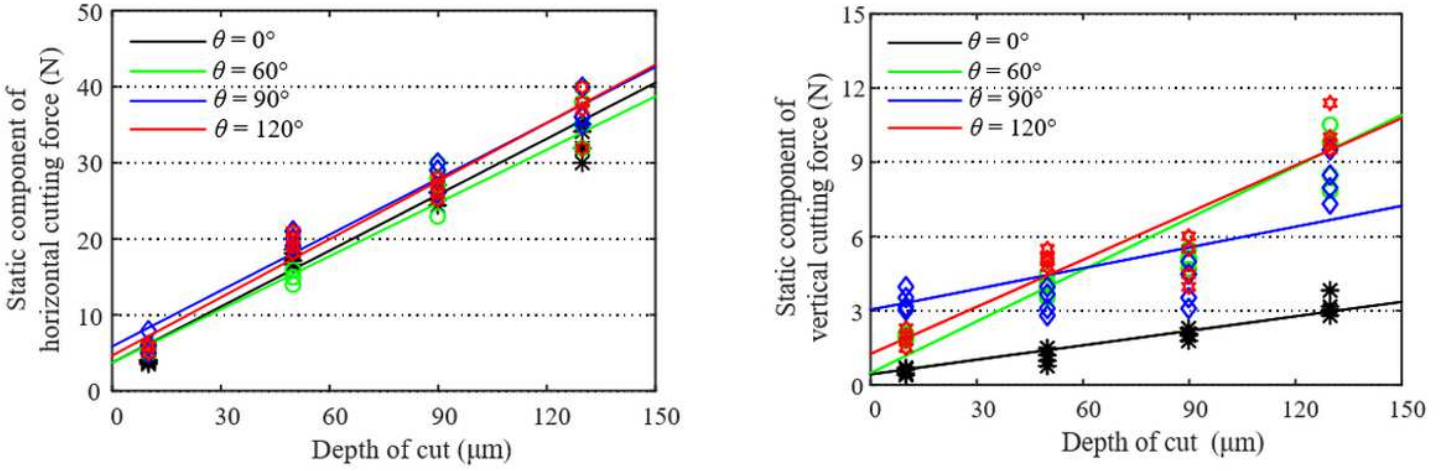

Figure 13

Static component of cutting force versus the depth of cut

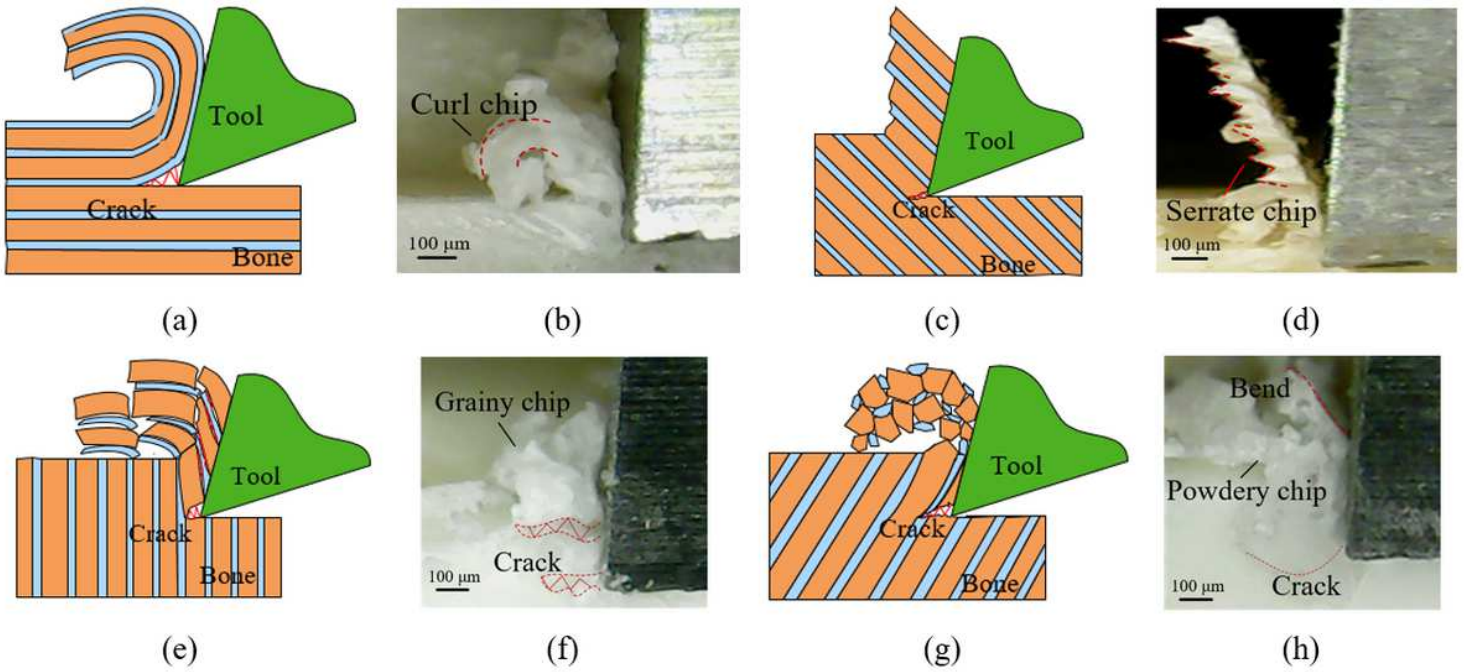

Figure 14

Chip formations in depth of cut 130 μm: (a) cutting model for mode #1, (b) curl chip in mode #1, (c) cutting model for mode #2, (d) serrated chip in mode #2 (e) cutting model for mode #3, (f) grainy chip in mode #3, (g) cutting model for mode #4, and (h) powdery chip in mode #4

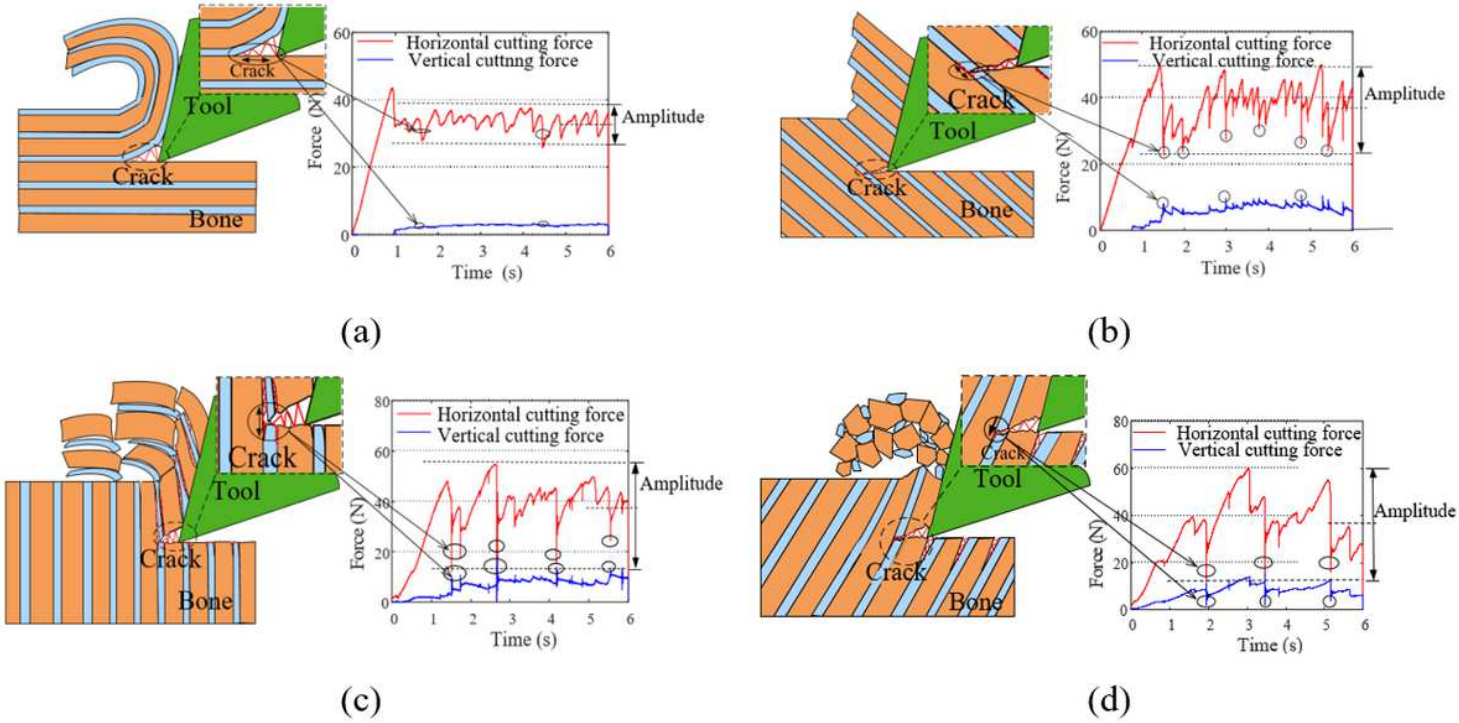

Figure 15

Crack propagations and cutting forces when the depth of cut was set as 130 μm: (a) mode #1, (b) mode #2, (c) mode #3 (d) mode #4